Available online at www.sciencedirect.com

ScienceDirect

Geochimica et Cosmochimica Acta 166 (2015) 1–14

Geochimica et Cosmochimica Acta

www.elsevier.com/locate/gca

Zircon $^4He/^3He$ thermochronometry

Alka Tripathy-Lang *, Matthew Fox, David L. Shuster

Department of Earth and Planetary Science, 307 McCone Hall, University of California, Berkeley, CA 94720, USA
Berkeley Geochronology Center, 2455 Ridge Road, Berkeley, CA 94709, USA

Received 6 December 2014; accepted in revised form 11 May 2015; Available online 22 May 2015

Abstract

Multiple thermochronometric methods are often required to constrain time-continuous rock exhumation for studying tectonic processes or development of km-scale topography at Earth's surface. Here, we explore $^4He/^3He$ thermochronometry of zircon as a method for constraining continuous time–temperature (t–T) paths of individual samples through a temperature range that is complementary to methods such as $^{40}Ar/^{39}Ar$ thermochronometry of K-feldspar and $^4He/^3He$ thermochronometry of apatite. For different cooling rates and diffusion domain size, the temperature sensitivity of zircon $^4He/^3He$ thermochronometry ranges from slightly less than 100 °C to slightly greater than 250 °C; a typical sample provides continuous thermal constraints over ~100 °C within that range. Outside these temperatures, ^4He in zircon will either be quantitatively retained or completely lost by volume diffusion. As proof-of-concept, we present stepwise release $^4He/^3He$ spectra and associated U and Th concentration maps measured by laser ablation ICP-MS analysis of individual crystal aliquots of Fish Canyon Tuff (FCT) zircon and of a more complex setting in the Sierra Nevada batholith that experienced reheating from a proximal basaltic intrusion, the Little Devil's Postpile (LDP). The FCT zircon $^4He/^3He$ release spectra are consistent with a ^4He spatial distribution dominated by alpha-ejection from crystal surfaces. The spatial distributions of U and Th measured in the same crystals do not substantially influence $^4He/^3He$ release spectra that are predicted for the known thermal history, even when incorporating spatially variable diffusivity due to accumulation of radiation damage. Conversely, the LDP $^4He/^3He$ release spectra are strongly influenced by the observed parent nuclide zonation. A three-dimensional (3D) numerical model of ^4He production and diffusion, which incorporates crystal geometry, U and Th zonation, and spatially variable He diffusion kinetics, substantially improves the fit between measured and modeled $^4He/^3He$ release spectra for the independently known thermal history of the sample. We conclude that zircon $^4He/^3He$ thermochronometry provides accurate thermal constraints through geologic time, but certain applications of this technique may require 3D numerical modeling approaches.

1. INTRODUCTION

Quantitative constraints on time-continuous geologic thermal paths of individual minerals arise from knowledge of the spatial concentration distribution of radiogenic daughter products that experience diffusive loss (e.g. Harrison et al., 2005). Such methods typically constrain aspects of the thermal path that are not obtainable solely via conventional bulk analyses of various thermochronometric systems. For example, apatite $^4He/^3He$ thermochronometry involves stepwise degassing analyses to measure the spatial distribution of ^4He within the apatite

Abbreviations: CL, Cathodoluminescence; FCT, Fish Canyon Tuff; Dt/a^2, diffusion kinetics; eU, effective uranium, $eU = [U] + 0.235[Th]$; FT, fission track; F_T, fraction of alpha particles that come to rest within a crystal; LAICPMS, laser ablation inductively coupled plasma mass spectrometry; LDP, Little Devil's Postpile; r, radial coordinate; R_{step}, $^4He/^3He$ ratio of each step; R_{bulk}, the $^4He/^3He$ ratio of the bulk sample; t–T, time–temperature; T_{bc}, bulk closure temperature; T_o, opening temperature; T_r, resetting temperature.

* Corresponding author at: Department of Earth and Planetary Science, 307 McCone Hall, University of California, Berkeley, CA 94720, USA. Tel.: +1 512 289 0753.

E-mail address: atripathy@bgc.org (A. Tripathy-Lang).

http://dx.doi.org/10.1016/j.gca.2015.05.027
0016-7037/

crystal with respect to a uniform distribution of proton-induced ^{3}He. These data constrain permissible thermal paths between temperatures of ~30 and 90 °C, which corresponds to shallow crustal depths of approximately 1–3 km and, therefore, can be related to the evolution of the subsurface thermal field due to km-scale topographic changes (e.g. Shuster and Farley, 2004; Schildgen et al., 2010; Shuster et al., 2011). At greater temperatures and depths, ^{40}Ar/^{39}Ar thermochronometry of K-feldspar via multi-diffusion domain modeling constrains continuous paths between ~200 and 350 °C, which can be related to tectonically-driven phenomena (e.g. Lovera et al., 1997; Harrison et al., 2005). In principle, continuous cooling paths at temperatures between these two systems should be attainable from ^{4}He/^{3}He thermochronometry of zircon, although non-uniform spatial distribution of parent nuclides in zircon imposes significant complexity on the system (Hourigan et al., 2005). However, if the spatial distribution of U and Th is observed within an individual crystal, combined knowledge of the spatial distribution of ^{4}He production and ^{4}He/^{3}He degassing analysis of the same crystal would resolve an important gap in continuous time–temperature (t–T) histories of samples between ~100 and 200 °C. Furthermore, in cases where fission track (FT) studies may be able to span this temperature range, resolution may be limited by crystals with young FT ages or those low in uranium concentration. Such crystals may not have accumulated sufficient spontaneous fission tracks to obtain reliable track counting statistics (Donelick et al., 2005). Therefore, bridging this gap would resolve t–T paths of individual bedrock samples to link tectonic and geomorphic processes active over million year timescales.

Complexities in the (U–Th)/He system in apatite are caused in part by inhomogeneity in the spatial distributions of U and Th within individual crystals (Farley et al., 2011). Such complexities are likely exacerbated in zircon, which can be far more zoned in parent nuclide concentration than apatite (e.g. Hourigan et al., 2005; Dobson et al., 2008). In turn, inhomogeneous U and Th distributions cause multiple complications. First, the alpha particles produced along U and Th decay chains have kinetic energies that propel them ~18 μm in zircon (Hourigan et al., 2005). At the grain boundary, a statistical proportion of the alpha particles are ejected from the grain, which requires that (U–Th)/He ages be corrected for ^{4}He loss (~$1/F_T$, where F_T is the fraction of alpha particles that come to rest within a crystal; Farley et al., 1996). While algorithms exist for accommodating complex zonation (Hourigan et al., 2005), the spatial distribution is rarely measured, making such corrections difficult. This results in unquantifiable errors in the F_T correction related to both the proportion of ^{4}He ejected from the grain boundary and the fact that the daughter product does not reside near the parent. Furthermore, the local diffusivity of ^{4}He within the crystal may change through both space and time due to differences in the degree of radiation damage (Farley et al., 2011; Guenthner et al., 2013; Fox et al., 2014). In turn, different zones within the crystal will release different amounts of ^{4}He during each step of a degassing experiment. In summary, ^{4}He/^{3}He zircon thermochronometric data are sensitive to the cooling history the crystal experienced, the spatial distribution of ^{4}He production and the spatial distribution of radiation damage. All of these factors can play an important role in obtaining accurate t–T paths.

Cathodoluminescence (CL) can be used to examine zonation of U and Th in zircon, but is only a proxy for concentration. Though it is possible to extract quantitative information from individual zones using an ion microprobe (Dobson et al., 2008), this exercise is both time- and cost-intensive. Recent studies have demonstrated that for apatites zoned in U and Th concentration, zonation can be quantitatively mapped using laser ablation-inductively coupled plasma mass spectrometry (LA-ICPMS; Farley et al., 2011), with the observation that LA-ICPMS is a more reliable measure of U and Th concentration in apatite than CL (Ault and Flowers, 2012). We propose that zircon can be treated similarly to zoned apatite and mapped for U–Th concentrations in the same manner.

In this study, we first explore the theoretical sensitivity of the zircon ^{4}He/^{3}He thermochronometer by focusing on various thermal histories and zoning patterns using standard ^{4}He diffusion kinetics in zircon (Reiners et al., 2004). We then present empirical tests of this method using samples from two field sites with independently known thermal histories – Fish Canyon Tuff (e.g. Reiners et al., 2002) and Little Devil's Postpile (e.g. Calk and Naeser, 1973). The analytical methods involve coupling ^{4}He/^{3}He step-wise degassing analyses with the spatial distribution of parent nuclide concentrations determined via LA-ICPMS analysis of polished sections of the same crystals, measured after the ^{4}He/^{3}He analysis. We present such data from three grains of Fish Canyon Tuff to test the method and illustrate the continuous thermal information that is constrainable within the t–T window that serves as the boundary conditions derived from existing geologic constraints. We then show data from the country rock adjacent to Little Devil's Postpile, a basaltic plug in the Sierra Nevada, where additional complexities related to the non-monotonic thermal history and zonation highlight the utility of incorporating site-specific diffusivity (Fox and Shuster, 2014) using the zircon radiation damage model (Guenthner et al., 2013) coupled with a 3D model of the zircon crystal (Fox et al., 2014).

2. MODELED ZIRCON ^{4}He/^{3}He PROFILES

In this section, we use He diffusion kinetics of Reiners et al. (2004) (i.e., that does not evolve with radiation damage accumulation) to calculate forward models to illustrate the temperature sensitivity of zircon ^{4}He/^{3}He thermochronometry, and explore how U and Th zonation can influence the data.

2.1. Temperature sensitivity

We estimate the temperature sensitivity of the zircon ^{4}He/^{3}He thermochronometer with the opening and resetting temperatures (T_o and T_r), as defined by Gardes and Montel (2009). They formulate T_o and T_r to mirror the original closure temperature equation of Dodson (1973).

For the geometric constant A, Gardés and Montel maintain its dependence on geometry but incorporate retention into the constant, with the opening and resetting thresholds corresponding to 1% and 99% loss of daughter nuclide (^{4}He in this case). For a radius of 60 μm, a cooling rate of 10 °C/Ma, and ^{4}He diffusion parameters in zircon from Reiners et al. (2004), T_o is 118 °C and T_r is 215 °C, whereas the nominal bulk closure temperature (T_{bc}), calculated from Dodson (1973) is 180 °C. We thus expect ^{4}He/^{3}He data that is observable via sequential degassing (Shuster et al., 2004) to be sensitive to temperatures bounded by T_o and T_r. Fig. 1 shows both T_o (solid) and T_r (dashed) for a range of radii and several reasonable cooling rates. The temperature sensitivity ranges from <100 °C to >250 °C, with a typical grain yielding information over a ~100 °C span within that range. In Fig. 2, we show forward models for two arbitrary and complicated t–T paths that only overlap within the gray box defined by T_o and T_r. Zircons from both t–T paths yield the same results in a ^{4}He/^{3}He step-wise degassing experiment because above T_r, complete diffusive loss of ^{4}He dominates the system, and below T_o, the ^{4}He diffusion profile will be effectively closed to diffusive loss and hence be dominated by alpha ejection.

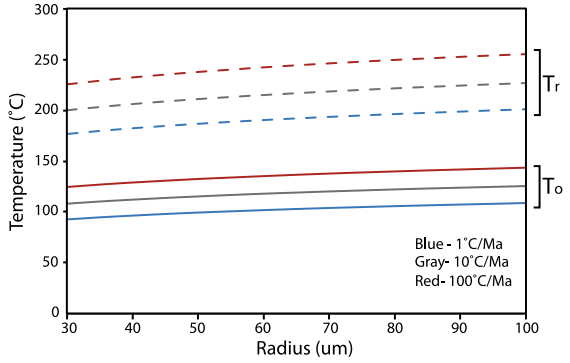

Fig. 1. Curves showing opening (solid) and resetting (dashed) temperatures, T_o and T_r, respectively, as a function of diffusion domain radius, calculated using the equations in Gardes and Montel (2009) and the diffusion kinetics of Reiners et al. (2004).

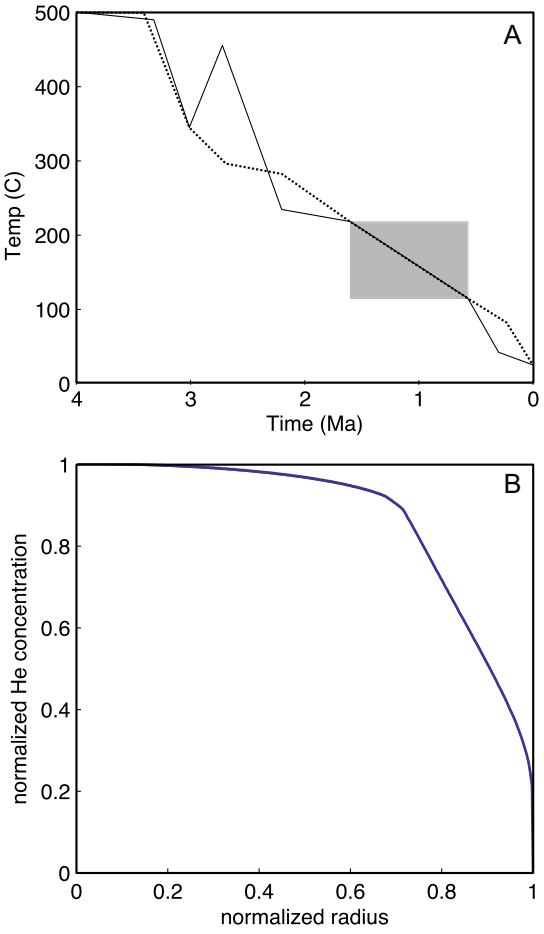

Fig. 2. (A) Two arbitrary and distinct time–temperature paths that overlap only within the temperature sensitivity range of the zircon ^{4}He/^{3}He thermochronometer (gray box). (B) Resultant He concentration profiles from both paths are indistinguishable.

2.2. Forward modeling of unzoned zircons

We use forward models with t–T paths like those of Shuster and Farley (2004; their Fig. 3) to predict zircon ^{4}He/^{3}He spectra for different cooling conditions. These t–T paths include rapid cooling, constant cooling at a relatively slow cooling rate, and extended residence at a constant temperature (i.e., within the partial retention zone) followed by recent instant cooling (Fig. 3a). Each thermal history results in an F_T-corrected (U–Th)/He age of 28 Ma for the diffusion parameters of Reiners et al. (2004), yet the ^{4}He/^{3}He ratio evolution diagrams (Fig. 3c) predicted from each ^{4}He concentration profile (Fig. 3b) are distinct and resolvable from one another.

The steady-state ^{4}He distribution (solid curve) that results after sufficiently long residence at a nearly constant temperature (~150 °C in this case), is highly diffusive and shows no obvious alpha ejection effect because diffusion is the dominant mechanism of ^{4}He loss at this temperature and tends to smooth and obscure the alpha ejection profile. On the other hand, the rapid cooling profile (dashed) is dominated by alpha ejection, as evidenced by the distinct kink in the concentration profile. The constant cooling profile ($dT/dt = 5.3$ °C/Ma; dotted) lies in between, being more rounded because of diffusion, but still displaying the alpha ejection-related kink. In the ratio evolution diagrams, the rapid and constant cooling profiles are similar, with the most marked differences in the first 10% of gas released (Fig. 3c, inset).

2.3. Forward modeling of zoned zircons

In the context of the same t–T paths, we explore how zonation affects the spatial distribution of ^{4}He and observable ratio evolution diagrams (Fig. 4) using four idealized patterns of eU zonation (eU = [U] + 0.235[Th] from Silver and Deutsch, 1963; Flowers et al., 2007). The top row shows three zonation patterns – high-eU core (Fig. 4a), high-eU rim (Fig. 4b) and oscillatory zoning (Fig. 4c). In all cases, the bulk eU is 247 ppm. The second

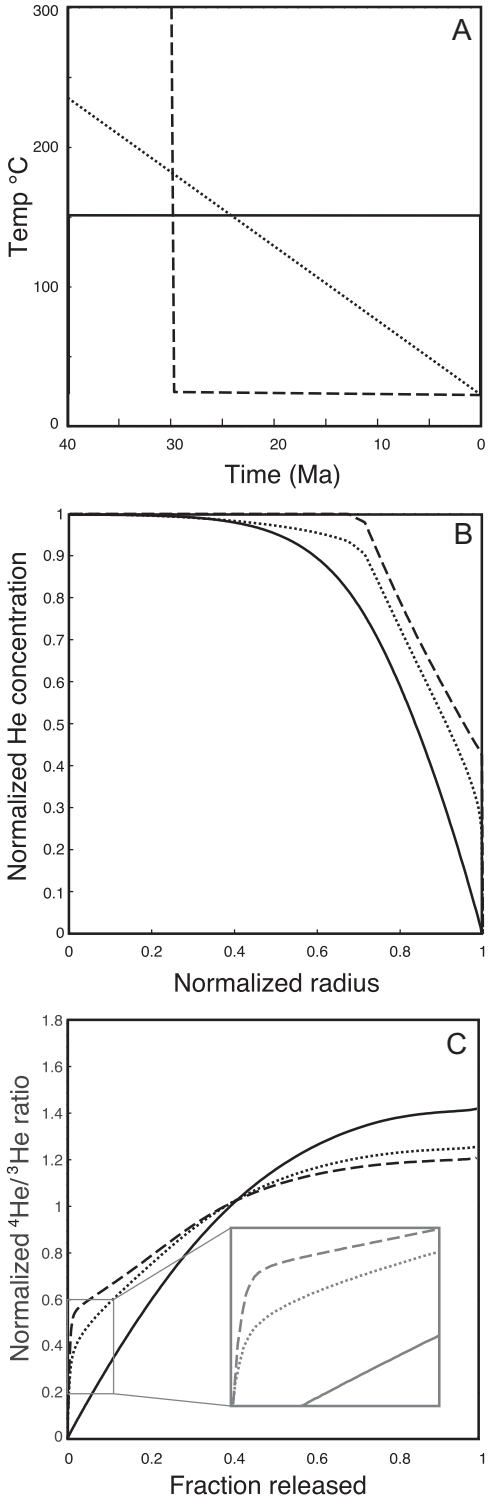

Fig. 3. (A) Three different time–temperature paths, which all yield a zircon (U–Th)/He age of 28 Ma. (B) ^{4}He concentration profiles for each t–T path. (C) Ratio evolution diagram for each t–T path. R_{step} is the ^{4}He/^{3}He ratio of each step, and is normalized to the ^{4}He/^{3}He ratio of the bulk sample (R_{bulk}) as a function of cumulative fraction of ^{3}He released during sequential degassing (Shuster and Farley, 2004). Solid = residence at constant temperature followed by instantaneous cooling recently, dashed = rapid cooling rate, and dotted = constant slow cooling rate.

row (Figs. 4d–f) shows the predicted ^{4}He/^{3}He ratio evolution diagrams that would result for each eU pattern and for each of the cooling paths in Fig. 3. In the third row, we show the corresponding ^{4}He concentration profiles (Fig. 4g–i).

2.3.1. Steady state

The steady state case (Fig. 3a, solid line) highlights two important aspects of the zircon (U–Th)/He system. First, the unzoned and oscillatory-zoned cases have nearly identical ^{4}He concentration profiles (Fig. 4g, black versus green curve), and indistinguishable ratio evolution diagrams (Fig. 4d, green curve directly atop black curve). This predicts that oscillatory zoning should not substantially influence an observable ^{4}He/^{3}He spectrum, provided that the characteristic length scale of eU oscillation is similar to the range of radiogenic alpha particle redistribution in zircon. Conversely, either high-eU cores or high-eU rims (i.e., zonation with a length scale significantly larger than the alpha particle range) will strongly affect the ^{4}He/^{3}He spectrum. In the high-eU core example (red curve), the ^{4}He concentration profile decreases toward the rim somewhat linearly, whereas a local maximum appears at a radial distance of ~0.7 in the high-eU rim example (blue curve, Fig. 4g).

2.3.2. Rapid cooling

The rapid cooling case (Fig. 3a, dashed curve) differs from the steady state case in several ways. First, the unzoned and oscillatory-zoned cases have different ^{4}He concentration profiles (Fig. 4h, black versus green curves). Furthermore, all concentration profiles show a distinct kink at a radial distance of ~0.7, which corresponds to part of the profile dominated by probabilistic alpha emission from the edge of the crystal. This manifests as a rapid rise in the normalized ^{4}He/^{3}He ratio evolution in the first 1–2% of released He (Fig. 4e). This indicates that the initial steps in a stepwise degassing experiment are very important in deciphering the correct thermal history. Importantly, the ratio evolution diagrams for both the unzoned and oscillatory cases are again indistinguishable (Fig. 4e, green line atop black line), which implies that regardless of thermal history, certain oscillatory zonation patterns will not significantly influence ^{4}He/^{3}He spectra.

2.3.3. Constant cooling

The constant cooling case (Fig. 3a, dotted line) is similar to the rapid cooling case. In the normalized concentration profiles (Fig. 4i), the kink related to alpha ejection is less sharply defined due to diffusive rounding while the grain cooled through the T_r–T_o window. This translates to the first few steps in the ratio evolution diagram being more rounded than in the rapid cooling case (Fig. 4f), further reinforcing that the initial steps in a stepwise degassing experiment are important for constraining the cooling history.

2.3.4. Summary

The above discussion highlights that the spatial distribution of U and Th within zircon can strongly influence the

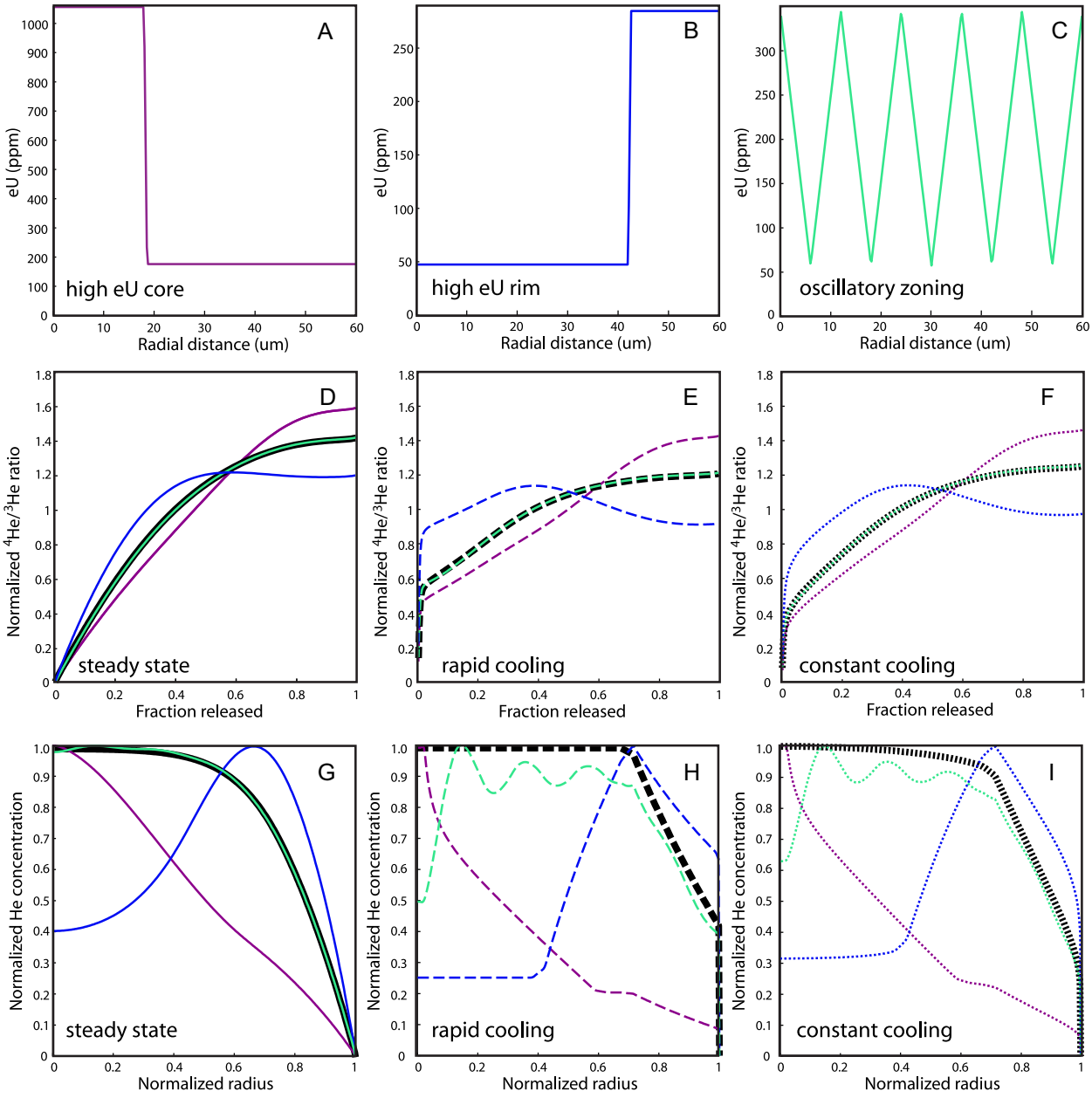

Fig. 4. (A–C) shows different zoning profiles used to calculate the ratio evolution diagrams (D–F, respectively) and normalized He concentration profiles (G–I) for each t–T path shown in Fig. 3A. The thick black curves in D–I (which are nearly identical to the green curves in D–G) show the results for spatially uniform eU. All calculations use the He diffusion kinetics of Reiners et al. (2004). (For interpretation of the references to color in this figure legend, the reader is referred to the web version of this article.)

^{4}He distribution resulting from different geologic cooling paths. Additionally, if zonation is not identified, the F_T-corrected bulk (U–Th)/He age may change as a result of zoning pattern (e.g. Guenthner et al., 2013). As expected, the unzoned and oscillatory cases yield essentially the same bulk (U–Th)/He age of 28 Ma in all the t–T paths shown in Fig. 3a. However, because the $1/F_T$ correction assumed a spatially uniform distribution of parent nuclides, the corrected (U–Th)/He ages are between 29 and 31 Ma for the high-eU core case because excess daughter is retained relative to parent, and between 22 and 25 Ma for the high-eU rim case because of increased ejection of ^{4}He at the rim. The latter case causes the largest deviation from the age in the unzoned case, which is expected as per Hourigan et al. (2005), but these authors provide a method to correct such erroneous ages using the zonation pattern.

The calculations also indicate that unzoned grains and those with oscillatory zoning can yield indistinguishable ^{4}He/^{3}He spectra (Fig. 4d–f), regardless of their similar or dissimilar concentration profiles (Fig. 4g–i). Furthermore, the initial steps of a stepwise degassing experiment are important for distinguishing thermal histories.

3. SAMPLE SELECTION

3.1. Fish Canyon Tuff

As an initial test of zircon ^{4}He/^{3}He thermochronometry, we use zircon crystals from Fish Canyon Tuff (FCT). FCT is widely used as an internal consistency test for zircon (U–Th)/He dating because it cooled rapidly, minimizing complexities introduced by diffusive loss of ^{4}He (Reiners, 2005). Although the canonical eruption age of FCT has varied over the past few decades, the most recent estimate is 28.196 ± 0.038 Ma (Wotzlaw et al., 2013), with previous studies obtaining a range of ages, from 27.89 to 28.305 Ma (e.g. Renne et al., 2010; Westerhold et al., 2012).

FCT zircon is highly zoned in U and Th concentrations (Schmitz and Bowring, 2001; Dobson et al., 2008), likely because of its protracted crystallization history (e.g. Bachman et al., 2007). There are six different types of zonation patterns, characterized by Dobson et al. (2008) using CL. The most common types show broadly concentric oscillatory zoning with different core-rim relationships. The remaining types include those with fluid or mineral inclusions such as alkali feldspars and quartz (Reiners et al., 2002), and grains that have simple zonation patterns that can be approximated as step functions. The least common population contains grains with homogeneous CL intensity, implying that in this case, homogenous distribution of U and Th is the exception rather than the rule.

3.2. Little Devil's Postpile

Little Devil's Postpile (LDP), in Yosemite National Park, is a small basalt plug, ~100 m across, that was intruded into the Cathedral Peak Granodiorite of the Sierra Nevada batholith. It is the site where Calk and Naeser (1973) showed how the intrusion systematically reset both the apatite and titanite fission track thermochronometers in the country rock. The crystallization age of 88.1 ± 0.2 Ma was determined by zircon U–Pb geochronology (Coleman and Glazner, 1997). 1.5 m from the intrusion, both apatite and titanite yield fission track ages of 9.4 ± 0.2 Ma, whereas 150 m from the intrusion, both thermochronometers record the background cooling age of the country rock, 80.7 ± 0.7 Ma. At intermediate distances is a zone of partial resetting (Calk and Naeser, 1973). In our study, the sample of interest (LDP1005), which has been partially reset, is located 4.5 m from the contact and yields a zircon (U–Th)/He age of *ca.* 31 Ma, whereas a sample located 63 m from the contact yields the background zircon (U–Th)/He cooling age of *ca.* 80 Ma (Table S1, see Supplementary Materials for analytical method).

4. METHODS

4.1. ^{4}He/^{3}He isotope measurement

Zircon grains were irradiated with a total fluence of ~1.0×10^{16} p/cm^2 with incident energy of ~220 MeV over a continuous ~5 h period at the Francis H. Burr Proton Therapy Center at the Massachusetts General Hospital (Shuster et al., 2004). After proton irradiation, grains of zircon were analyzed in the BGC Noble Gas Thermochronometry Lab. Individual crystals were loaded into Pt–Ir packets and sequentially degassed under static vacuum at different temperatures using a 70 W diode laser controlled in a feedback loop with a pyrometer. After each heating step, the extracted gas was purified with a SAES GP-50 getter pump fitted with C-50 cartridge (St101 alloy), and the remaining gas was condensed onto activated charcoal within a temperature-controlled cryogenic trap held at 11 K. Helium was then released from the trap at 33 K and analyzed using a MAP-215 mass spectrometer. The ^{3}He abundance and ^{4}He/^{3}He ratio were measured using pulse-counting (^{3}He) and Faraday cup (^{4}He) sector field mass spectrometry calibrated against reference gas standards and corrected for blank contributions to ^{3}He and ^{4}He, as described in Shuster et al. (2012) and Tremblay et al. (2014). After sequentially heating each sample, we observed abundances at the maximum extraction temperature of less than 1% of the total amount of ^{3}He and ^{4}He observed throughout the total sequence of extractions; this indicates that nearly all ^{3}He and ^{4}He was extracted from each sample.

4.2. U and Th isotope measurement and data reduction

U and Th isotope measurements were obtained using an Analyte G2 laser coupled with a Thermo Scientific Neptune Plus ICPMS at the Berkeley Geochronology Center. Following the ^{4}He/^{3}He analyses, euhedral zircon crystals were mounted in epoxy with their *c*-axes parallel to the mount. They were polished following procedures typical for electron microprobe work, and mapped on a grid of line-scans both parallel and perpendicular to the *c*-axis. Data for concentration maps were collected in a similar manner to apatite, as described by Farley et al. (2011). Each traverse began and ended in epoxy to ensure analysis of the entire grain, and the Analyte G2 recorded precise *x*–*y* locations along each line-scan at 2-s increments. The laser was operated at 5 Hz with a spot diameter of 20 μm at 30% energy output. Typical fluence was 2.27 J/cm^2. Line-scans were executed at a rate of approximately 1 μm/s.

Ablated material was analyzed for ^{238}U, ^{232}Th and ^{91}Zr. These isotopes were selected in order to minimize interferences and maximize signal intensity for precise measurement on the Faraday collectors. Before and after each set of scans per grain, gas blanks were measured, averaged and subtracted from the data. Typical gas blanks were less than 0.2 mV for each isotope. ^{91}Zr intensity from each line scan was used to determine when the laser completely intersected the zircon, as indicated by a rapid rise and stabilization of the signal intensity. A rapid decrease in signal intensity was used to identify the opposite edge of each crystal (Farley et al., 2011). For each cycle, we computed the ratios ^{238}U/^{91}Zr and ^{232}Th/^{91}Zr from the blank-corrected signals. Each cycle is offset from the previous by a distance of 3.7 μm, based on the 1 μm/s traverse rate and cycle time of 3.7 s.

To quantify U and Th concentrations in material ablated from samples, we used reference zircon 91500, from

Kuehl Lake, Ontario, Canada (Wiedenbeck et al., 2004) and measured $^{238}U/^{91}Zr$ and $^{232}Th/^{91}Zr$ ratios across a 100-μm line scan under the same operating conditions both before and after every sample. The mean ratios for each line scan were converted to sensitivities by dividing them by known ^{238}U and ^{232}Th concentrations of 80 ± 10 ppm and 29.9 ± 7 ppm, respectively, from Wiedenbeck et al. (2004). Because the goal is primarily to obtain relative rather than absolute concentrations, minor variations of U and Th concentrations in the 91500 zircon standard are not of concern. We then multiply observed sample ratios by these sensitivities [e.g. sensitivity expressed as ppm $^{238}U/(^{238}U/^{91}Zr)$] in an equivalent manner to Farley et al. (2011) by assuming a spatially uniform distribution of ^{91}Zr in both the standard and unknown. We then calculate the effective uranium concentration (eU) that weights the decay of both U and Th for their alpha particle production rates (Flowers et al., 2007). This results in a series of concentration determinations across each grain. The location of each ratio was determined by comparing the timestamps along each line scan, collected every 2 s, and the timestamp corresponding to each individual ratio. To estimate the error associated with the U and Th concentration measurements for the unknowns, we calculate eU values for all cycles across each standard traverse. The typical variability is ~7% at the 1 sigma level, which we consider a reasonable error estimation in this application.

The resulting grid of concentrations is then processed using an inverse distance weighting (IDW) algorithm with a power parameter of 0.7 and a radial distance limit of 20–40 μm. The data are interpolated at a mesh size of 2 μm × 2 μm, and plotted as color ramp contour plots of eU. The main parameter controlling the average length-scale is the 20–40 μm radius neighborhood used to calculate the concentration at each point along the uniformly-spaced concentration grid (Farley et al., 2011). Each ratio is collected at a spacing of approximately 4 μm, well within the 20–40 μm averaging window. We also processed the grid of concentrations using an ordinary kriging algorithm with an exponential model. Because the forward modeling results are indistinguishable, we consider the computationally faster IDW method sufficient for our purposes. See Supplementary Material for comparison between the two interpolation methods.

Finally, in order to convert an eU concentration map into an eU zoning profile that can be used by simple ^4He production-diffusion models, the 2D eU concentration map is collapsed onto a single 1D radial coordinate, which we refer to as a spherical equivalent eU profile (Farley et al., 2011).

5. RESULTS FROM FCT ZIRCON

5.1. $^4He/^3He$ step-heating experiments

The results of $^4He/^3He$ step-heating experiments on three different crystals of FCT zircon are shown in Fig. 5. For ease of comparison, we superimpose a predicted $^4He/^3He$ spectrum for several different cases, using the known cooling history for FCT and observed eU zonation for each crystal as discussed below, in Section 5.3. In all examples, the resultant spectra are qualitatively consistent with an alpha-ejection dominated profile with some diffusive rounding.

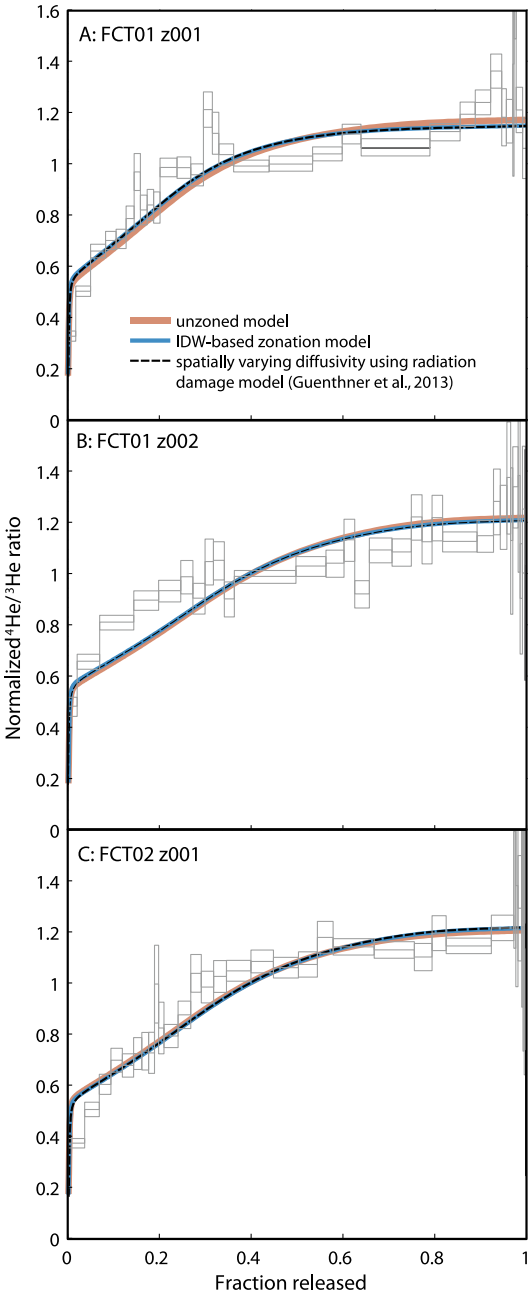

Fig. 5. $^4He/^3He$ release spectra for three different zircon crystals from Fish Canyon Tuff. The height of each box is the analytical uncertainty of each measurement. Solid curves are model spectra calculated for instant cooling at the time of eruption assuming (i) spatially uniform eU (red curves) and (ii) the observed zonation in eU for each crystal shown in Fig. 6 using the IDW-derived zonation models and diffusion kinetics from Reiners et al. (2004) (solid blue curves), or the radiation damage model (Guenthner et al., 2013) (dashed black curves). Axes are the same as in Fig. 3C. (For interpretation of the references to color in this figure legend, the reader is referred to the web version of this article.)

In Fig. 5a, the $^4He/^3He$ spectrum is concave down between release fractions 0.2–0.4, and concave up between 0.4 and 0.85. This pattern mimics that of Fig. 4e, which implies that the rim is enriched in U and/or Th concentration relative to the core. In Fig. 5b, the $^4He/^3He$ spectrum is concave down between release fractions 0.05–0.3, and then is slightly concave up from 0.45 to 0.75, when compared to the unzoned prediction. This is again similar to Fig. 4e, suggesting that this grain also has a high-eU rim. Although the general pattern between Figs. 5a and b are similar and predict a high-eU rim, they are distinct in detail, suggesting that their zoning patterns will be only roughly comparable. Fig. 5c appears to be the result of either no zoning or oscillatory zoning, as per Fig. 4e. Based on the work of Dobson et al. (2008), we consider the latter case to be most likely. Interestingly, the experiment's only departure from the predicted spectra is in the first two steps, which indicates a low-eU rim.

5.2. eU concentration maps and spherical equivalent eU concentration profiles

Here, we discuss the eU contour maps and spherical equivalent eU concentration profiles of the same three crystals (Fig. 6) in the context of our predictions from the $^4He/^3He$ step-heating experiments.

In Fig. 6a, both the eU map and the profile indicate a high-eU rim, as predicted by the $^4He/^3He$ spectrum, although the high-eU rim is discontinuous in map view. In Fig. 6b, the map does not resolve any distinct core-rim relationship. Instead, there appears to be a low-eU zone in the lower part of the grain that indicates an offset core. The spherical equivalent eU concentration profile reveals a very subtle core-to-rim increase in eU. These findings agree with our expectation that this grain would display a different pattern than the first, but that overall, we would find a high-eU rim relationship. In Fig. 6c, the eU contour map indicates patchy zonation, with the spherical equivalent profile revealing a slight decrease in eU from core to rim. We are unable to confirm whether the grain displays oscillatory zoning from the eU contour map, which is not surprising considering the laser spot size of 20 μm and the scale of the zonation, between 15 and 20 μm (Dobson et al., 2008).

5.3. Forward modeling

As an initial test of the zircon $^4He/^3He$ method, we use the spherical equivalent concentration profiles in Fig. 6 to forward model $^4He/^3He$ spectra for the known thermal history of FCT, and compare these results with a model that assumes a uniform distribution of eU (Fig. 5). In each of the three zircons, the $^4He/^3He$ data are consistent with rapid cooling following the tuff eruption, and clearly exclude gradual cooling or prolonged residence above ~200 °C. Interestingly, despite the observed zonation in eU, the $^4He/^3He$ release spectra of all three aliquots are nearly consistent with models assuming a uniform eU distribution (Fig. 5). Thus, including the zonation pattern in the forward model does not appear to substantially

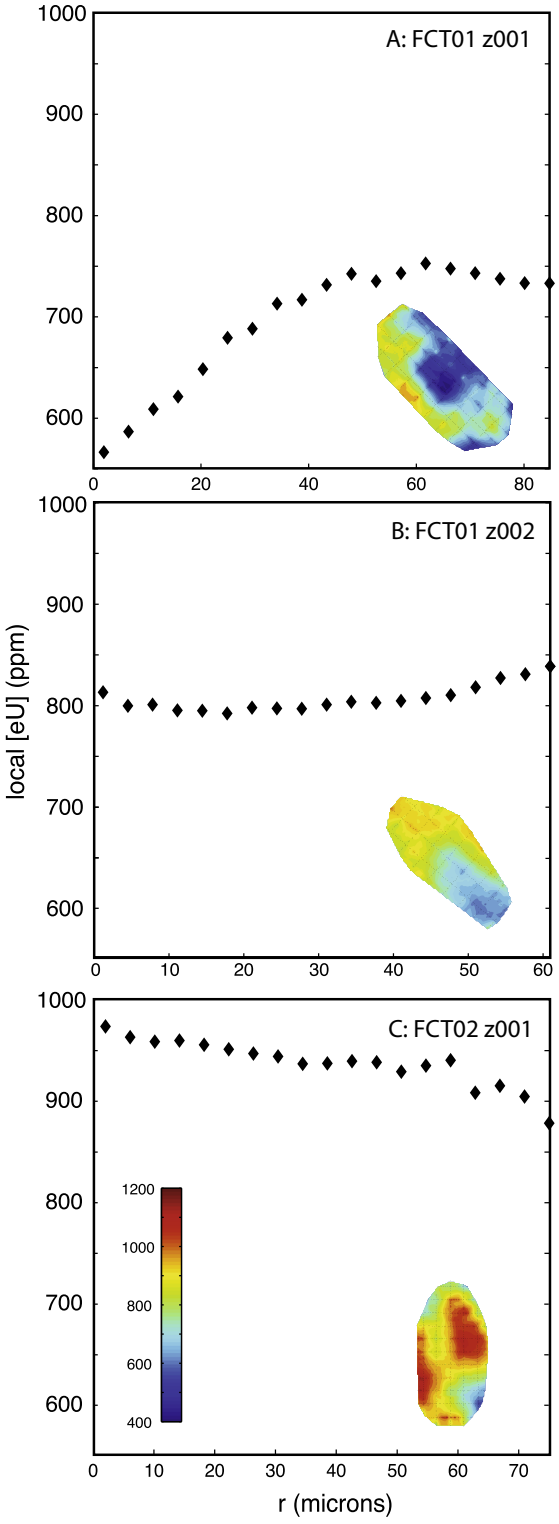

Fig. 6. Zonation patterns of eU for the three crystals shown in Fig. 5. The maps of eU (inset figures), observed by LA-ICPMS analysis, are converted into spherical models shown as local eU concentration ([eU]) plotted against a radial coordinate (r) using a conversion described in Farley et al. (2011). The color maps are all equivalently scaled, with the scale bar shown in (C). (For interpretation of the references to color in this figure legend, the reader is referred to the web version of this article.)

influence the predicted $^4He/^3He$ spectra in these cases, even when including spatially variable diffusivity using the Guenthner et al. (2013) radiation damage model (Fig. 5).

These results indicate that regions of lower ^4He productivity in these zircons approximately balance the regions of higher ^4He productivity within the crystals. While this is not the general case, this balance likely arises because both the ^4He production and diffusion occur over length scales and with stochasticism that "blurs" some of the fine scale structure of U and Th distributions in each crystal. Further, the rapid cooling of FCT may have minimized complexities expected for spatially variable diffusion kinetics (Guenthner et al., 2013), as evidenced by the black dashed model in Fig. 5.

In these forward models, the *t–T* paths do not fully reproduce all of the characteristics of the $^4He/^3He$ spectra (Fig. 5). Despite the blurring effects described above, the fine-scale spatial complexity in eU zonation may render the 1D spherical equivalent model insufficient in certain applications and specific zircons, which we will discuss in more detail in Section 6.

We can further test the utility of $^4He/^3He$ zircon thermochronometry by searching time–temperature space for cooling histories that are consistent with the data (see Shuster et al., 2011). In Fig. 7a, we begin all forward model calculations well before the known crystallization age of FCT zircon to explore whether the data are able to constrain reasonable *t–T* paths in the appropriate temperature sensitivity range (Fig. 7a, red box) without knowledge of the crystallization time. Most randomly selected paths do not pass the fit criteria (gray paths) except for those with rapid cooling between *ca.* 33 and 27 Ma (green paths), as expected. The red vertical line at 30 Ma highlights the approximate crystallization age, and interestingly, only a single predicted *t–T* path fits the data (bold blue path), and is the correct result based on preexisting knowledge of Fish Canyon Tuff. When we begin the model at 30 Ma, the only *t–T* paths that result in good fits are those in which rapid cooling occurs between 30 and 27 Ma to temperatures below 120 °C (Fig. 7b). This highlights that the time when the model begins is important for correctly constraining the cooling path of a given sample, as shown for apatite

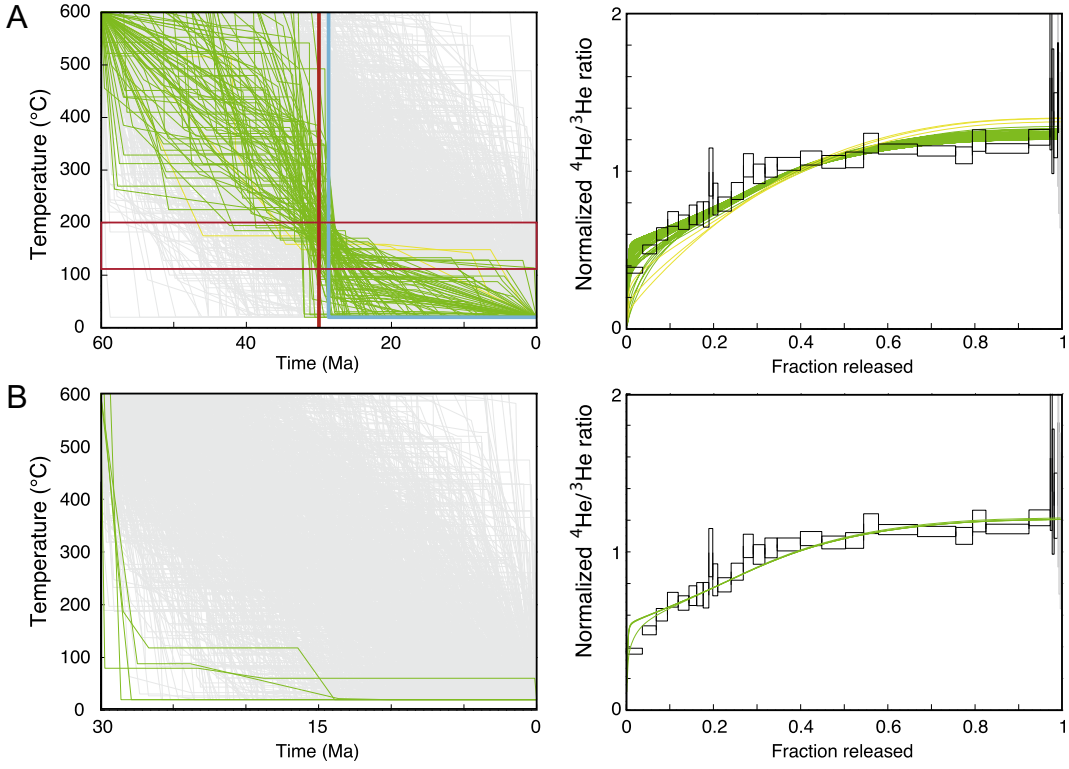

Fig. 7. Thermal constraints using the data of crystal FCT02-z001 (Fig. 5c) identified from 1000 randomly generated time–temperature paths, and assuming spatially uniform eU and the He diffusion kinetics of Reiners et al. (2004). Green, yellow and gray paths show the randomly generated cooling paths. Green paths predict a good fit to the data, whereas yellow paths predict worse fits that can be excluded at a 99% confidence level based on our statistical assessment (see Schildgen et al. (2010) for detailed discussion). Gray paths indicate modeled cooling paths that failed to predict the observed (U–Th)/He age. Between 6 and 10 nodes are used to describe the time temperature paths, and temperature is forced to decrease through time, i.e., reheating is not permitted. Plots on right show the predicted $^4He/^3He$ data for the corresponding green and yellow cooling paths. (A) All cooling paths begin at 60 Ma and 600 °C, and end at 0 Ma and 25 °C. Red box indicates range of approximate temperature sensitivity. Bold vertical red line indicates approximate crystallization age. Bold blue path highlights the single *t–T* path that fits both the observations and the known geologic history. (B) All cooling paths begin at 30 Ma and 600 °C, and end at 0 Ma and 25 °C. (For interpretation of the references to color in this figure legend, the reader is referred to the web version of this article.)

by Fox and Shuster (2014). Thus, we advocate incorporating established geologic constraints to set boundary conditions for any forward or inverse modeling exercise.

6. RESULTS FROM LDP ZIRCON

6.1. ^{4}He/^{3}He step-heating experiment

The results of ^{4}He/^{3}He step-heating experiments for LDP1005-z001 and LDP1005-z002 are shown as the gray steps in Fig. 8b and c. For ease of comparison, we superimpose modeled ^{4}He/^{3}He spectra for various cases using a simplified cooling history (Fig. 8a) that is derived from previous work (Calk and Naeser, 1973), and is consistent with the bulk zircon (U–Th)/He age for this sample, ~31 Ma (Supplementary Material, Table S1). At release fractions greater than 0.8, ^{4}He/^{3}He ratios are much higher than predicted, which indicates a very high-eU core.

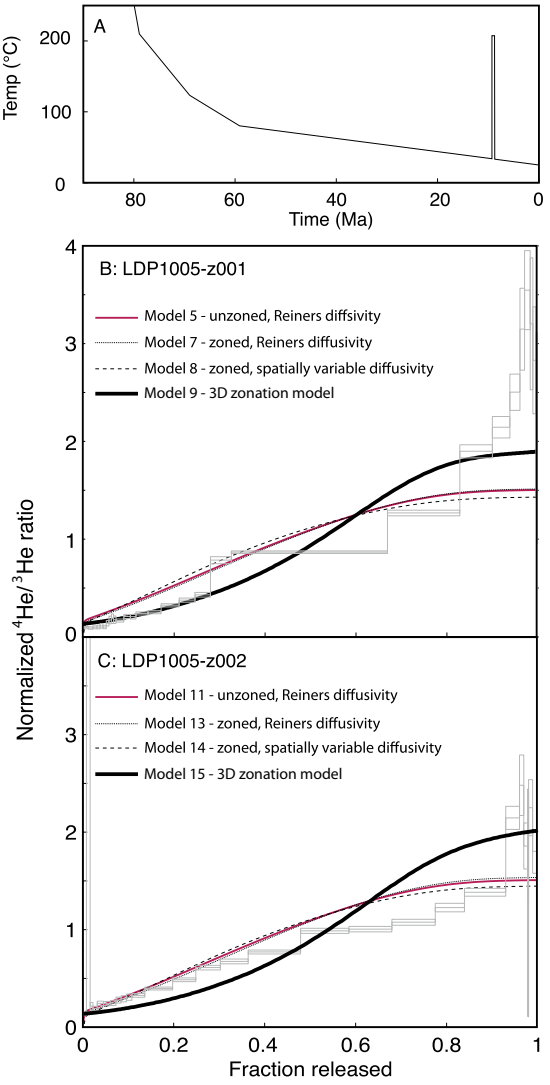

Fig. 8. Zircon ^{4}He/^{3}He thermochronometry of a sample that experienced late-stage reheating, LDP1005. (A) Time–temperature path used for modeling sample LDP1005, with square heating pulse at 9 Ma. Duration of heating event is 500 ka, and the maximum temperature was adjusted to between ~190 and 220 °C to ensure that the predicted zircon (U–Th)/He age agrees with the observed age of 31 Ma. (B–C) Observed ^{4}He/^{3}He release spectra for LDP1005-z001 (B) and -z002 (C) and results of forward models assuming spatially uniform eU (solid curves) and incorporating the observed eU zonation of each crystal shown in Fig. 9 (dashed curves). 3D models are shown as bold curves. All model parameters are listed in Supplementary Materials Table S2.

6.2. eU concentration map and spherical equivalent eU concentration profile

The eU contour maps and spherical equivalent eU concentration profiles for both crystals are shown in Fig. 9. The IDW-derived spherical equivalent eU concentration profiles average out much of the effects of the localized regions of high [eU] in each eU map. Interestingly, these high [eU] regions, particularly in Fig. 9b, have very high Th concentration relative to the surrounding zircon, which might indicate an inclusion such as monazite, a Th-rich phosphate. Importantly, the patterns of eU zonation for both crystals

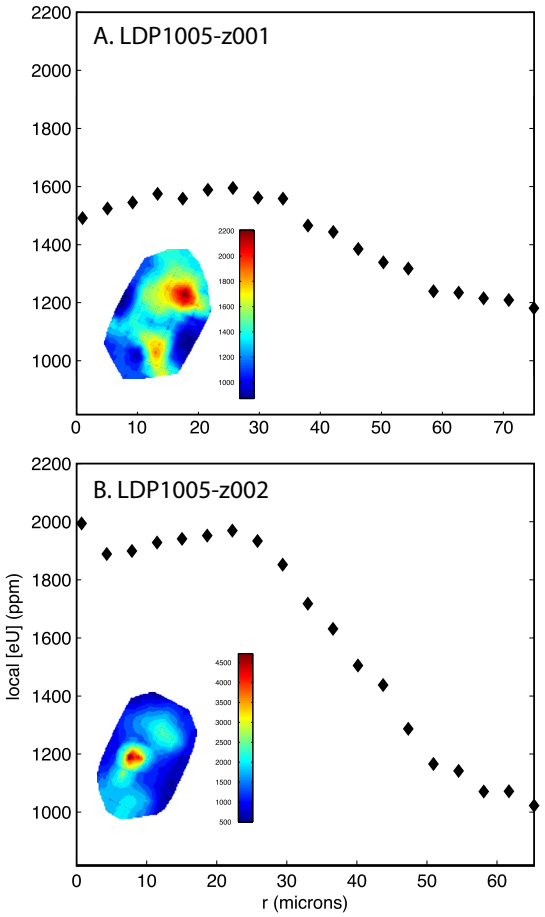

Fig. 9. Zonation patterns of eU for the two crystals shown in Fig. 8. The maps of eU (inset figures), observed by LA-ICPMS analysis, are converted into spherical models shown as local eU concentration ([eU]) plotted against a radial coordinate (r) using a conversion described in Farley et al. (2011). Note that the local [eU] axes and maps are at the same scale, but the radial coordinate axes differ based on crystal size.

are comparable, with zones containing much higher [eU] (>2000 ppm) slightly offset from center (Fig. 9a and b). These observations are broadly consistent with the predictions made from the $^4He/^3He$ spectra.

6.3. Forward modeling

In this section, we first discuss the results of spherical equivalent forward models, following Farley et al. (2011). We then show results from 3D forward modeling that follows the procedure of Fox et al. (2014).

6.3.1. Spherical equivalent models

The most important constraint on any given forward model is that it yields a bulk zircon (U–Th)/He age of ~31 Ma (Supplementary Table S1). Since our LA-ICPMS data primarily quantify relative differences in U and Th, to estimate the bulk [eU] of this sample, we hold this age constant and calculate the bulk [eU] that would correspond to this age and total observed ^4He. Variables in our forward models include the choice in diffusion kinetics (Reiners et al., 2004; Guenthner et al., 2013), duration of the heating event (0.1–0.5 Ma) and the time at which that event begins (9.0–9.4 Ma). Each time we change any one of these variables, a different maximum temperature must be selected in order to ensure that the resultant bulk zircon (U–Th)/He age remains 31 ± 5 Ma, i.e., to maintain the requisite Dt/a^2. Given a predicted age, the only variables that appear to affect the $^4He/^3He$ spectrum in any discernible way are the choice in diffusion kinetics model in conjunction with the zonation pattern.

Initially, we use the diffusion kinetics of Reiners et al. (2004) for an unzoned grain and the calculated average bulk eU concentrations. We increase the duration of the heating event from 0.1 Ma to 0.5 Ma, but because the resultant curves plot atop one other (Supplementary Materials, Fig. S8), we only show the result for a heating event of 0.5 Ma duration (Fig. 8b and c, Models 5 and 11). The same is true if we change the time at which the heating event began from 9.4 Ma to 9 Ma. For LDP1005-z001, the unzoned model does not replicate the shape of the $^4He/^3He$ spectrum very well, with only the middle part of the forward modeled profile, from 0.3 to 0.7, matching the $^4He/^3He$ spectrum. For LDP1005-z002, the unzoned profile matches the beginning of the release spectrum and closely follows the same pattern except between ~0.4 and 0.8 and the final steps of the $^4He/^3He$ spectrum.

When we incorporate zonation patterns from Fig. 9 with ^4He diffusion kinetics of Reiners et al. (2004), the forward models for LDP1005-z001 yield similar profiles to those without zonation (Fig. 8b, Model 7). However, for grain LDP1005-z002, including radial eU zonation better reproduces the beginning of the $^4He/^3He$ spectrum (Fig. 8c, Model 13). In these calculations, diffusivity is spatially uniform at any time, but the eU zonation causes non-uniform ^4He productivity.

By incorporating the Guenthner et al. (2013) radiation damage model, we can also account for the possibility of spatially varying diffusion kinetics as a function of radiation damage accumulation through time, and hence local [eU]. For both samples (Fig. 8b Model 8, Fig. 8c Model 14), the profile is similar to those derived using the Reiners et al. (2004) diffusion kinetics, which is expected because this crystal has neither sufficient prior history nor eU concentration to have accumulated enough radiation damage for the Guenthner et al. (2013) model to substantively influence the model spectrum.

To summarize, in LDP1005-z001, all spherical equivalent models do a poor job of predicting the measured $^4He/^3He$ spectrum. For both samples, each model fails to produce the sharp increase in $^4He/^3He$ ratios observed at >0.8 released. In part, this could be due to the process by which the 2D maps of eU concentration are converted to 1D spherical equivalent concentrations (Farley et al., 2011). This process averages eU as a function of distance from the edge of the crystal, resulting in a decrease in the range of eU values. Zones within the crystal with anomalous eU concentrations may strongly influence the $^4He/^3He$ release spectra by (1) producing more or less ^4He and (2) evolving different diffusional kinetics and hence temperature sensitivity due to radiation damage. These anomalous zones, in particular, may be averaged out by the conversion from 2D to 1D. The degree to which extreme values of eU are averaged depends on the spatial distribution of eU and whether the maps can be approximated by concentric zones (Fox et al., 2014). In the next section we reduce the effects of this averaging by creating a 3D model of the crystal, based on the 2D map, and solving the He production–diffusion equation for this model.

6.3.2. 3D forward modeling

In Fig. 8b and c, the solid, bolded curves are models calculated using a 3D representation of each crystal following the method of Fox et al. (2014), by interpolating the eU contour maps in both positive and negative z directions by the half-width of the crystal. We assign eU values equivalent to the average of the lowest 10 eU measurements made during LA-ICPMS analysis to the upper and lower surfaces of each crystal. Because we preserve the extreme values of eU observed in the map, we expect the effects of averaging to be reduced with respect to the spherical equivalent model. We use the Guenthner et al. (2013) radiation damage model to specify diffusivity at each location within the 3D model at each time step in our thermal model (Fig. 8a).

For LDP1005-z001, the 3D model (Fig. 8b Model 9) does an excellent job of predicting the $^4He/^3He$ spectrum in comparison to the profiles derived from the spherical models. However, this model still over-predicts one step at approximately 80% of the released gas, and under-predicts the final 10% of the measured spectrum. For LDP1005-z002, the 3D model (Fig. 8c; Model 15) replicates the end of the $^4He/^3He$ spectrum reasonably well where the spherical equivalent model fails; however, the first 80% of the spectrum, which contains more information about diffusive loss of ^4He in the field, appears to be better predicted by the spherical equivalent model (Fig. 8c; Model 14). This suggests that our 3D model does not accurately describe the crystal, and this may be due to several factors that are discussed in Section 7.2.

7. DISCUSSION

7.1. Geologic utility

Given its temperature sensitivity of <100 °C to >250 °C, zircon ^{4}He/^{3}He thermochronometry can address both surface process- and tectonics-related questions, and serve as a link between apatite ^{4}He/^{3}He thermochronometry and other higher temperature thermochronometers. Aside from the two examples provided here (i.e., a volcanic rock with a simple thermal history, and a granitic rock with a slightly more complicated cooling history than most), this method should be valuable for any application where bulk zircon (U–Th)/He dates are required. This includes extensional environments (e.g. Stockli, 2005), convergent and collisional margin settings (e.g. Biswas et al., 2007), and impact structures (e.g. Young et al., 2013). Furthermore, this can be coupled with apatite ^{4}He/^{3}He studies to constrain continuous thermal paths between temperatures less than 50 °C to above 200 °C, which in some cases may discriminate surface processes driven by climate variation (e.g. Shuster et al., 2011) versus tectonics. Zircon ^{4}He/^{3}He thermochronometry should also be valuable to studies requiring apatite fission track analysis when available apatites have insufficient fission track densities for reliable statistics. This includes grains that are simply too young and/or too low in eU. In addition, the overlapping temperature sensitivity of these systems, based on different assumptions and underlying processes, provides a means to check for consistency.

7.2. Potential complications

Because FCT and LDP are both relatively young and, in the case of FCT, cooled rapidly after eruption, it is unlikely to have been affected by several complications that might influence ^{4}He diffusion profiles in zircon, including anisotropic diffusion (e.g. Cherniak and Watson, 2009). In zircon, He appears to diffuse faster in the direction parallel to the *c*-axis. Both molecular dynamic simulations (e.g. Reich et al., 2007) and laboratory measurements using nuclear reaction analysis (Cherniak and Watson, 2009) have demonstrated this feature of zircon. However, Guenthner et al. (2013) observe an important co-variation between diffusional anisotropy and radiation damage. The less radiation damage they observe, the more important anisotropic diffusion appears to be, whereas an increased amount of radiation damage accumulation results in less diffusional anisotropy. This implies that radiation damage is a far more central control on diffusion of ^{4}He in zircon, and that anisotropy may be an added complexity in specific cases. Indeed, for grain LDP1005-z001 from Little Devil's Postpile (Fig. 8b), the radiation damage model, when coupled with U–Th zonation extrapolated into three dimensions, predicts much of the ^{4}He/^{3}He spectrum. However, for grain LDP1005-z002 (Fig. 8c), the radiation damage model coupled with 3D zonation of U–Th qualitatively fails to improve the fit between the measured and predicted ^{4}He/^{3}He spectrum, which might indicate that we may not sufficiently understand He diffusion in zircon and the influence of radiation damage.

An additional complication may be caused by inclusions, as might have been imaged in grain LDP1005-z002 (Fig. 9b). We caution that one must be careful to select crystals with the fewest inclusions to avoid difficulty in interpretation. In the future, it would be possible to incorporate changes in mineralogy into the 3D model, and this is an avenue of future research.

A related complication is that we do not image the entire crystal in 3D during eU contour mapping. We measure eU variations across a 2D plane within the crystal, and then extrapolate, using the assumptions discussed in Section 6.3.2, into a 3D model. An alternative strategy would be to collect and interpolate data from multiple surfaces at different depths within the crystal. This problem might be exacerbated by inclusions that appear as eU hotspots that do not intersect the measured plane, and are thus not accounted for in the model.

8. CONCLUSIONS

The work presented here explores the utility and limitations of ^{4}He/^{3}He thermochronometry of zircon. The temperature sensitivity of this system is between approximately 90 and 250 °C, depending on cooling rate, grain size, and assumed quantification of ^{4}He diffusion kinetics. In principle, the method should constrain continuous thermal histories within this temperature range. Like apatite ^{4}He/^{3}He thermochronometry, zircon ^{4}He/^{3}He release spectra can identify permissible geologic thermal paths of individual samples, but will generally require consideration of eU zonation patterns unless the grain displays symmetric oscillatory zonation. Finally, quantitative applications of the method will benefit from 3D zonation models that account for spatial complexity in ^{4}He production and diffusion as well as radiation damage effects on He diffusivity in zircon. However, 3D zonation models are not required in all cases, and sometimes produce less robust predictions of ^{4}He/^{3}He spectra than the spherical equivalent model. Because zircons commonly exhibit complex spatial distributions of U and Th, this adds leverage to constrain thermal conditions, especially when multiple crystals with variable zonation are analyzed from the same rock.

ACKNOWLEDGMENTS

We thank Warren Sharp and Nick Fylstra for invaluable assistance in the lab, and Greg Balco for assistance with the random search algorithm. Barry Kohn, an anonymous reviewer, and AE Alex Nemchin provided constructive suggestions that helped clarify several aspects of this paper. Funding was provided by the following sources: The National Science Foundation Petrology and Geochemistry Program (EAR-1049988 to DLS), and the Ann and Gordon Getty Foundation.

APPENDIX A. SUPPLEMENTARY DATA

Supplementary data associated with this article can be found, in the online version, at http://dx.doi.org/10.1016/j.gca.2015.05.027.

REFERENCES

Ault A. K. and Flowers R. M. (2012) Apatite U–Th zonation and thermochronology data interpretation. *Geochim. Cosmochim. Acta* **79**, 60–78.

Bachman O., Oberli F., Dungan M. A., Meier M., Mundil R. and Fischer H. (2007) $^{40}Ar/^{39}Ar$ and U–Pb dating of the Fish Canyon magmatic system, San Juan Volcanic field, Colorado: evidence for an extended crystallization history. *Chem. Geol.* **236**, 134–166.

Biswas S., Coutand I., Grujic D., Hager C., Stockli D. and Graseman B. (2007) Exhumation and uplift of the Shillong plateau and its influence on the eastern Himalayas: new constraints from apatite and zircon (U–Th–[Sm])/He and apatite fission track analyses. *Tectonics* **26**. http://dx.doi.org/10.1029/2007TC002125.

Calk L. C. and Naeser C. W. (1973) The thermal effect of a basalt intrusion on fission track in quartz monzonite. *J. Geol.* **81**, 189–198.

Cherniak D. J. and Watson E. B. (2009) Diffusion of helium in zircon and apatite. *Chem. Geol.* **268**, 155–166.

Coleman D. S. and Glazner A. F. (1997) The sierra crest magmatic event: rapid formation of juvenile crust during the late cretaceous in California. *Int. Geol. Rev.* **39**, 768–787.

Dodson M. H. (1973) Closure temperatures in cooling geological and petrological systems. *Contrib. Mineral. Petrol.* **40**, 259–274.

Dobson K. H., Stuart F. M. and Dempster T. J.EIMF (2008) U and Th zonation in Fish Canyon Tuff zircons: implications for a zircon (U–Th)/He standard. *Geochim. Cosmochim. Acta* **72**, 4545–4755.

Donelick R. A., O'Sullivan P. B. and Ketcham R. A. (2005) Apatite fission track analysis. In *Low-temperature Thermochronology: Techniques, Interpretations and Applications: Reviews in Mineralogy and Geochemistry* (eds. P. W. Reiners and T. A. Ehlers). vol. 58, pp. 49–94.

Farley K. A., Wolf L. T. and Silver L. T. (1996) The effects of long alpha-stopping distances on (U–Th)/He ages. *Geochim. Cosmochim. Acta* **60**, 4223–4229.

Farley K. A., Shuster D. L. and Ketcham R. A. (2011) U and Th zonation in apatite observed by laser ablation ICPMS, and implications for the (U–Th)/He system. *Geochim. Cosmochim. Acta* **75**, 4515–4530.

Flowers R. M., Shuster D. L., Wernicke B. P. and Farley K. A. (2007) Radiation damage control on apatite (U–Th)/He dates from the Grand Canyon region, Colorado Plateau. *Geology* **35**, 447–450.

Fox M. and Shuster D. L. (2014) The influence of burial heating on the (U–Th)/He system in apatite: Grand Canyon case study. *Earth Planet. Sci. Lett.* **397**, 174–183.

Fox M., McKeon R. E. and Shuster D. L. (2014) Incorporating 3-D parent nuclide zonation for apatite $^{4}He/^{3}He$ thermochronometry: an example from the Appalachian Mountains. *Geochem. Geophys. Geosyst.* **15**. http://dx.doi.org/10.1002/2014GC005464.

Gardes E. and Montel J.-M. (2009) Opening and resetting temperatures in heating geochronological systems. *Contrib. Mineral. Petrol.* **158**, 185–195.

Guenthner W. R., Reiners P. W., Ketcham R. A., Nasdala L. and Giester G. (2013) Helium diffusion in natural zircon: Radiation damage, anisotropy, and the interpretation of zircon (U–Th)/He thermochronology. *Am. J. Sci.* **313**, 145–198.

Harrison T. M., Grove M., Lovera O. M. and Zeitler P. K. (2005) Continuous thermal histories from inversion of closure profiles. In *Low-temperature Thermochronology: Techniques, Interpretations and Applications: Reviews in Mineralogy and Geochemistry* (eds. P. W. Reiners and T. A. Ehlers). vol. 58, pp. 389–410.

Hourigan J. K., Reiners P. W. and Brandon M. T. (2005) U–Th zonation-dependent alpha-ejection in (U–Th)/He chronometry. *Geochim. Cosmochim. Acta* **69**, 3349–3365.

Lovera O. M., Grove M., Harrison T. M. and Mahon K. I. (1997) Systematic analysis of K-feldspar $^{40}Ar/^{39}Ar$ step heating results: I. Significance of activation energy determinations. *Geochim. Cosmochim. Acta* **61**, 3171–3192.

Reich M., Ewing R. C., Ehlers T. A. and Becker U. (2007) Low-temperature anisotropic diffusion of helium in zircon: implications for zircon (U–Th)/He thermochronometry. *Geochim. Cosmochim. Acta* **71**, 3119–3130.

Reiners P. W. (2005) Zircon (U–Th)/He thermochronometry. In *Low-temperature Thermochronology: Techniques, Interpretations and Applications: Reviews in Mineralogy and Geochemistry* (eds. P. W. Reiners and T. A. Ehlers). vol. 58, pp. 151–179.

Reiners P. W., Farley K. A. and Hickes H. J. (2002) He diffusion and (U–Th)/He thermochronometry of zircon: initial results from Fish Canyon Tuff and Gold Butte. *Tectonophysics* **349**, 297–308.

Reiners P. W., Spell T. L., Nicolescu S. and Zanetti K. A. (2004) Zircon (U–Th)/He thermochronometry: He diffusion and comparisons with $^{40}Ar/^{39}Ar$ dating. *Geochim. Cosmochim. Acta* **68**, 1857–1887.

Renne P. R., Mundil R., Balco G., Min K. and Ludwig K. R. (2010) Joint determinations of ^{40}K decay constants and $^{40}Ar^{*}/^{40}K$ for the Fish Canyon sanidine standard, and improved accuracy for $^{40}Ar/^{39}Ar$ geochronology. *Geochim. Cosmochim. Acta* **74**, 5349–5367.

Schildgen T. F., Balco G. and Shuster D. L. (2010) Canyon incision and knickpoint propagation recorded by apatite $^{4}He/^{3}He$ thermochronometry. *Earth Planet. Sci. Lett.* **293**, 377–387.

Schmitz M. D. and Bowring S. A. (2001) U–Pb zircon and titanite systematics of the Fish Canyon Tuff: an assessment of high-precision U–Pb geochronology and its application to young volcanic rocks. *Geochim. Cosmochim. Acta* **65**, 571–587.

Shuster D. L. and Farley K. A. (2004) $^{4}He/^{3}He$ Thermochronometry. *Earth Planet. Sci. Lett.* **217**, 1–17.

Shuster D. L., Farley K. A., Sisterson J. M. and Burnett D. S. (2004) Quantifying the diffusion kinetics and spatial distributions of radiogenic ^{4}He in minerals containing proton-induced ^{3}He. *Earth Planet. Sci. Lett.* **217**, 19–32.

Shuster D. L., Cuffey K. M., Sanders J. W. and Balco G. (2011) Thermochronometry reveals headward propagation of erosion in an alpine landscape. *Science* **332**, 84–88.

Shuster D. L., Farley K. A., Vasconcelos P. M., Balco G., Monterio H. S., Waltenberg K. and Stone J. O. (2012) Cosmogenic ^{3}He in hematite and goethite from Brazilian "canga" duricrust demonstrates the extreme stability of these surfaces. *Earth Planet. Sci. Lett.* **329**, 41–50.

Silver L. T. and Deutsch S. (1963) Uranium–lead isotopic variations in zircons: a case study. *J. Geol.* **71**, 721–758.

Stockli D. F. (2005) Application of low-temperature thermochronometry to extensional tectonic settings. In *Low-temperature Thermochronology: Techniques, Interpretations and Applications: Reviews in Mineralogy and Geochemistry* (eds. P. W. Reiners and T. A. Ehlers). vol. 58, pp. 411–448.

Tremblay M. M., Shuster D. L. and Balco G. (2014) Diffusion kinetics of ^{3}He and ^{21}Ne in quartz and implications for cosmogenic noble gas paleothermometry. *Geochim. Cosmochim. Acta* **142**, 186–204.

Westerhold T., Rohl U. and Laskar J. (2012) Timescale controversy: accurate orbital calibration of the early Paleogene. *Geochim. Geophys. Geosyst.* **13**. http://dx.doi.org/10.1029/2012GC004096.

Wiedenbeck M. et al. (2004) Further characterisation of the 91500 zircon crystal. *Geostand. Geoanal. Res.* **28**, 9–39.

Wotzlaw J.-F., Schaltegger U., Frick D. A., Dungan M. A., Gerdes A. and Gunther D. (2013) Tracking the evolution of large-volume silicic magma reservoirs from assembly to supereruption. *Geology* **41**, 867–870.

Young K. E., van Soest M. C., Hodges K. V., Watson E. B., Adams B. A. and Lee P. (2013) Impact thermochronology and the age of the Haughton impact structure, Canada. *Geophys. Res. Lett.* **40**, 3836–3840.

Associate editor: Alexander Nemchin